NK cell co-localization with epithelial cells in pancreatic cancer is influenced by fibroblasts and ECM components

Zoe X. Malchiodi[1*], Alexander A. Lekan[1*], Robert K. Suter[1], Atul Deshpande[2,3,4], Ivana Peran[1], Brent T. Harris[5,6], Anju Duttargi[5], Min-Ju Chien[1], Samika Hariharan[1], Lucia Wetherill[1], Selime Arslan[1], Rachael Maynard[1], Annabel J. Lee[1], Annie Zuo[1], Sandra A. Jablonski[1], Won Jin Ho[2], Marwa Afifi[1], Elana J. Fertig[2,7,8,9], Louis M. Weiner[1]

[1] Department of Oncology, Georgetown Lombardi Comprehensive Cancer Center, Georgetown University Medical Center, Washington, DC, USA

[2] Department of Oncology, Sidney Kimmel Comprehensive Cancer Center, Johns Hopkins School of Medicine, Baltimore, MD, USA

[3] Department of Electrical and Computer Engineering, Johns Hopkins University, Baltimore, MD, USA

[4] Data Science and AI Institute, Johns Hopkins University, Baltimore, MD, USA

[5] Department of Pathology, Georgetown University Medical Center, Washington, DC, USA

[6] Department of Neurology, Georgetown University Medical Center, Washington, DC, USA

[7] Department of Applied Mathematics and Statistics, Johns Hopkins University Whiting School of Engineering, Baltimore, MD, USA

[8] Department of Biomedical Engineering, Johns Hopkins University School of Medicine, Baltimore, MD, USA

[9] Department of Medicine, University of Maryland School of Medicine, Baltimore, MD, USA

*These authors contributed equally to this work.

Address correspondence to: Louis M. Weiner, MD, Georgetown Lombardi Comprehensive Cancer Center, Research Building E501, 3970 Reservoir Rd NW, Washington, DC, 20057.
E-mail: weinerl@georgetown.edu.

27 **Graphical Abstract**

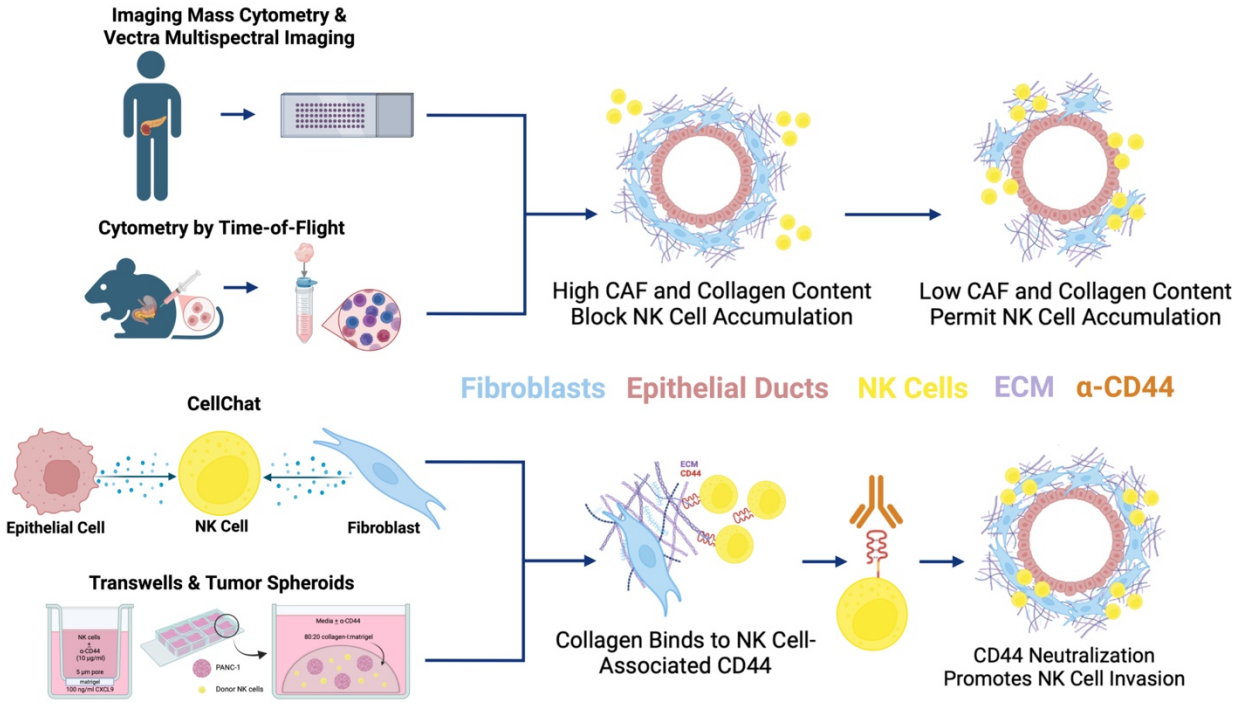

28

Abstract

Pancreatic ductal adenocarcinoma (PDAC) is the most aggressive and common type of pancreatic cancer. PDAC has a dense, fibrotic tumor microenvironment (TME) that restricts immune cell infiltration and contributes to poor immunotherapy responses. While T cell-based therapies have been largely ineffective, natural killer (NK) cells—which kill tumor cells without requiring MHC recognition—offer a promising alternative. However, their role in the PDAC TME remains poorly understood. Here, we show that NK cells are present, active, and spatially associated with malignant epithelial cells in human PDAC. Using cytometry by time-of-flight (CyTOF) in murine PDAC, imaging mass cytometry (IMC) in human tumors, and CellChat analysis of a human PDAC scRNAseq dataset, we found that NK cells interact with extracellular matrix (ECM) components via CD44. Fibroblast-rich, desmoplastic regions appear to limit NK cell infiltration. *In vitro* 2D and 3D assays revealed that CD44 neutralization significantly enhances NK cell matrix invasion. These findings highlight the underappreciated presence and tumor cell-proximal localization of NK cells in PDAC and identify ECM-CD44 interactions as a barrier to their infiltration. Targeting these interactions may enhance NK cell-based immunotherapy in PDAC.

Introduction

Pancreatic ductal adenocarcinoma (PDAC) is the most common form of pancreatic cancer, with a 5-year survival rate of 12%[1]. PDAC is slated to become the 2nd most common contributor to cancer-related deaths by 2030, thus there is a need for the identification of novel therapeutic approaches[2]. PDAC is considered to be immunologically "cold" as its tumor microenvironment (TME) is primarily desmoplastic as a result of extracellular matrix (ECM) production by cancer-associated fibroblasts (CAFs), accounting for at least 50% of the tumor volume[3]. This causes resistance to therapies, poor immunogenicity, and lack of activated immune cell infiltration[4,5]. Therefore, resolution of intratumoral cellular interactions within the PDAC TME is essential to identifying novel therapeutic approaches to treat this disease.

Natural killer (NK) cells remain critically understudied in pancreatic ductal adenocarcinoma (PDAC), despite their therapeutic relevance and prognostic significance. Unlike T cells, NK cells can kill tumor cells independent of antigen presentation, making them uniquely suited to bypass PDAC's immunosuppressive mechanisms[6]. Yet, while the PDAC tumor microenvironment (TME) has been extensively profiled for T cell and myeloid interactions[7,8,9,10,11,12], the spatial organization, functional states, and microenvironmental constraints on NK cells remain largely uncharacterized. This knowledge gap is especially consequential given our recent findings that higher NK cell infiltration correlates with significantly improved survival in PDAC patients and is required for tumor control in preclinical models[13]. Without a detailed understanding of how NK cells are positioned, regulated, and restricted within the PDAC stroma, it remains unclear whether—and how—they can be harnessed for therapeutic benefit. Our study addresses this unmet need by combining high-dimensional spatial and functional profiling to

define NK cell localization, activation, and interaction with the ECM in human and murine PDAC.

Here, we used multiple approaches to investigate the spatial and functional relationships of NK cells within the murine and human PDAC TME. First, we performed imaging mass cytometry (IMC), a high-dimensional spatial proteomics platform that maintains tissue architecture while capturing single cell data[14], and found that that activated NK cells co-localize and form close interaction networks with malignant epithelial cells in human PDAC tumors. Importantly, this spatial association was inversely correlated with fibroblast abundance and Collagen I expression, suggesting that ECM-rich regions exclude NK cells. Second, we analyzed immune cell infiltration in two KPC-derived, orthotopic murine PDAC models (KP1 and mT3-2D) using cytometry by time-of-flight (CyTOF), which revealed consistent NK cell infiltration, confirming their presence across model systems. Third, we applied CellChat—a ligand-receptor interaction inference tool— to a publicly available human PDAC single-cell RNA-seq dataset, and identified a previously undescribed interaction between CD44 on NK cells and collagens expressed by malignant epithelial cells and fibroblasts. Based on this, we hypothesized that ECM–NK cell interactions restrict NK cell invasion. In 2D and 3D *in vitro* collagen-containing matrix assays, CD44 neutralization significantly enhanced NK cell invasion. These findings demonstrate that the PDAC TME limits NK cell access via ECM-derived cues and reveal CD44 as a modifiable barrier to NK cell infiltration and potential therapeutic translation.

92 **Results**

93 **Spatial proteomic analysis of the human PDAC TME resolves PDAC cell populations**

94 To resolve the spatial landscape of the human PDAC TME, we performed IMC, on a
95 tissue microarray (TMA) of primary tumor samples from 21 treatment-naive PDAC patients. We
96 used a custom 40-marker metal-conjugated antibody panel targeting epithelial, immune, and
97 stromal lineages (**Supplementary Table S1**), and acquired 44 high-resolution pseudoimages
98 across patients' cores of primary tumor samples from 21 treatment-naive PDAC patients
99 (**Supplementary Table S2**). Using CyTOF technology, tissue images are reconstructed with
100 single cell resolution to enable higher order single cell proteomic and spatial analyses[14,15]
101 Following a known IMC cell segmentation pipeline[16] (**Fig. 1A**), we identified 412,862 cells in 44
102 IMC pseudoimages from these patients. Single-cell protein expression data were extracted for
103 downstream single-cell proteomic and spatial analyses[17]. Using Seurat-based analysis,
104 expression data was log-normalized and cell populations were identified using supervised
105 clustering approaches[18]. Canonical cell phenotype markers (CD11b, CD16, CD20, CD3,
106 CD45RO, CD4, CD56, CD68, CD8α, E-cadherin, FAP, NKG2D, αSMA, Pan-cytokeratin,
107 Vimentin) were used to distinguish between immune cells, epithelial cells, and fibroblasts during
108 cell clustering, which identified 8 predominant cell types (**Figs. 1B-C**): αSMA^+ fibroblasts, B
109 cells, $CD4^+$ T cells, $CD8^+$ T cells, epithelial cells, FAP^+ fibroblasts, macrophages, and NK cells.
110 These main cell types were then subclustered to identify the functional state of these cell
111 populations using the remaining markers in our IMC panel (**Supplementary Table S1**), and we
112 identified 29 distinct clusters to define active, proliferative, and apoptotic cell states
113 (**Supplementary Fig. S1**). As expected in PDAC, the majority of cells were fibroblasts and
114 epithelial cells, and we were able to define distinct immune cell populations, including NK cells

115 (**Figs. 1D-F**). We also observed that within our patient samples that there was a similar

116 proportion of NK cells to that of CD4$^+$ and CD8$^+$ T cell populations, suggesting the potential

117 relevance of NK cells in the human PDAC TME (**Fig. 1D**).

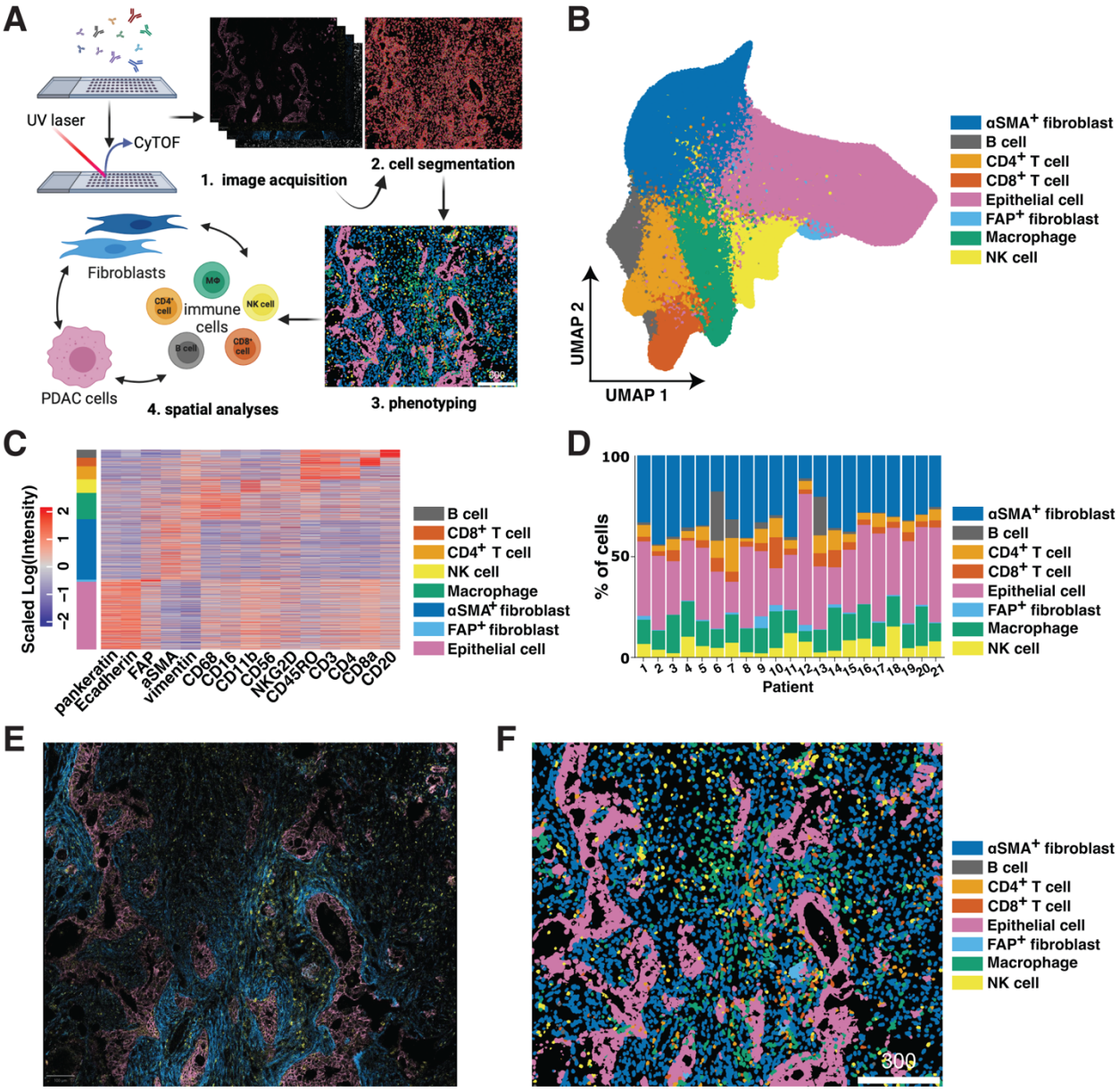

118

119 **Figure 1: Spatial proteomic analysis of the human PDAC TME resolves PDAC cell**

120 **populations. A.** Schematic of IMC workflow. **B.** UMAP of IMC-defined cell populations from

121 21 untreated PDAC patient samples. **C.** Heatmap of scaled log-normalized protein expression

122 intensities of canonical marker expression used to phenotype segmented human PDAC cell
123 populations. 15k cells randomly subsampled from the 21 PDAC patient samples are displayed.
124 **D.** Bar plot showing percentages of cell populations per PDAC patient. **E.** Representative IMC
125 pseudoimage of the human PDAC TME highlighting distinctions between epithelial cells (Pan-
126 cytokeratin and E-cadherin; pink), fibroblasts (αSMA and FAP; blue), and immune cells
127 (CD45RO; yellow). **F.** Single cell image (Cytomapper) of **E** displaying all identified cell types
128 from **B**-**D**.
129
130 **NK cells and epithelial cells co-localize and interact in murine and human PDAC TME**
131 We next sought to define the spatial interactions of NK cells within the human PDAC
132 TME using IMC. Qualitative evaluation of the IMC images revealed that NK cells co-localized
133 with epithelial cells in the human PDAC TME (**Fig. 2A**), which we confirmed using multiplex
134 immunofluorescence (IF) on 26 additional human PDAC samples (**Figs. 2B–C, Supplementary**
135 **Fig. S2**). To systematically quantify spatial relationships, we performed a cellular neighborhood
136 analysis[19] to classify distinct multi-cellular structures based on their functional status and cellular
137 interactions[19]. This analysis identified eight distinct cellular neighborhoods (**Supplementary**
138 **Fig. S3**). Notably, cellular neighborhoods 2 and 6 marked epithelial-ductal regions, with
139 neighborhood 2 highly enriched in both epithelial and NK cells (**Supplementary Figs. S3A**-**B**).
140 Interestingly, within these epithelial-ductal zones, NK cells were more abundant than $CD4^+$ or
141 $CD8^+$ T cells (**Supplementary Figs. S3–S4**), suggesting a preferential NK–tumor cell spatial
142 association. Conversely, epithelial-ductal regions featuring proliferative-epithelial cells, from
143 cellular neighborhood 6, had more cells from cellular neighborhood 5, which was rich in αSMA^+
144 fibroblasts (**Supplementary Figs. S3–S4**). These observations suggest that fibroblast-rich

145 regions support epithelial cell proliferation and prevent immune cell infiltration, supporting the
146 concept that fibroblasts act as immune decoys or deterrents in the PDAC TME.

147 Fibroblast composition also influenced neighborhood architecture; neighborhood 4
148 (immune-rich) surrounded epithelial areas with apoptotic features, while neighborhood 5
149 (αSMA^+ fibroblast-rich) was associated with regions of epithelial and fibroblast proliferation,
150 suggesting that fibroblast-rich zones support tumor cell growth and hinder immune access.
151 Neighborhood 8, containing active NK cells, had the second highest abundance of apoptotic
152 epithelial cells, further implicating NK cells in direct anti-tumor responses. Strikingly,
153 neighborhood 2 also exhibited the highest abundance of $IFN\gamma^+$ epithelial cells, with NK cells
154 being the dominant immune population present (**Supplementary Fig. S4**). These observations
155 support the hypothesis that NK cells are cytotoxic to malignant epithelial cells in human PDAC
156 and demonstrate that spatial analysis identifies NK cell-epithelial cell co-localization.

157 To test for specific cellular interactions, we conducted a permutation-based interaction
158 analysis[17]. Notably, this demonstrated that NK cells significantly interacted with apoptotic
159 epithelial cells more than $CD8^+$ T cells (**Fig. 2D**)—a previously undescribed finding in PDAC.
160 Euclidean distance analysis[8,20] further confirmed that NK cells, but not $CD8^+$ T cells, were
161 closely associated with epithelial cells, while αSMA^+ fibroblasts were the nearest stromal
162 population to NK cells (**Fig. 2E**), raising the possibility that fibroblasts may spatially restrict
163 NK–tumor engagement. A cell–cell network analysis[8] reinforced these findings: NK cell nodes
164 clustered around epithelial and apoptotic epithelial cell nodes but were spatially distant from T
165 cell nodes (**Fig. 2F**), highlighting the distinct localization and potential cytotoxic role of NK cells
166 in the PDAC TME.

167 To corroborate the presence of NK cells observed by IMC and Vectra, we performed
168 CyTOF analysis of infiltrating immune cells in two orthotopic, KPC-derived murine PDAC
169 tumor models (**Fig. 3**): KP1 *(LSL-Kras^{G12D}/Trp53$^{flox/+}$/p48-CRE)* and mT3-2D *(Kras$^{+/LSL-G12D}$;*
170 *Trp53$^{+/LSL-R172H}$; Pdx1-Cre)*[21]. Using an unsupervised density-based clustering approach, t-
171 distributed stochastic neighbor embedding (t-SNE)[22], we visualized the immune populations
172 present in each model (**Figs. 3C, 3G**), with cell identities assigned based on canonical lineage
173 markers (**Supplementary Fig. S5**). A total of 27 immune subsets were identified through
174 established gating strategies[23] (**Supplementary Fig. S6**).
175 NK cells (NK1.1^{+}, NKp46^{+}) were consistently present in both tumor models, representing
176 a prominent innate immune component despite the overall immunosuppressive
177 microenvironment (**Figs. 3D, 3H**). In contrast, CD4^{+} and CD8^{+} T cells, while present, were
178 phenotypically distinct across models—naïve (CD44^{-}CD62L^{+}) in KP1 tumors and exhausted
179 (PD-1^{+}) in mT3-2D tumors (**Supplementary Fig. S7)**, suggesting a differential capacity for
180 adaptive immune responses. B cells and granulocytic populations dominated the CD45^{+} fraction,
181 while dendritic cells were also present, primarily as conventional type 2 dendritic cells (cDC2).
182 These findings align with IMC and multiplex IF data that highlight NK cells as consistent and
183 spatially localized effectors within the tumor microenvironment of KPC-derived PDAC models.
184 Their presence, independent of T cell infiltration and functionality, suggests that NK cells may
185 represent a viable target for immunotherapeutic intervention in pancreatic cancer.

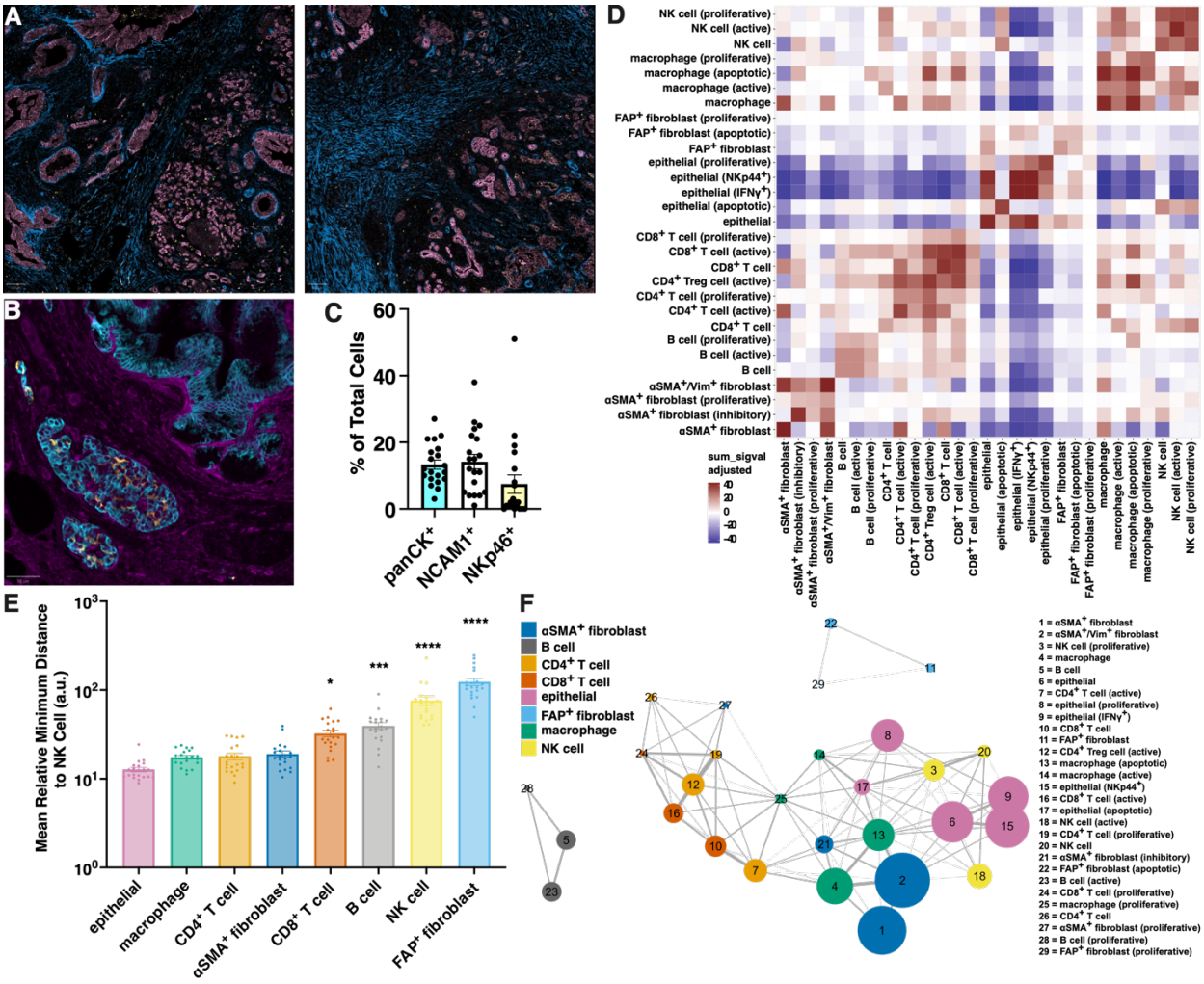

Figure 2: NK cells co-localize and interact with epithelial cells in the human PDAC TME. **A.** Representative IMC pseudoimages displaying NK cell-epithelial cell co-localization (αSMA = blue; E-cadherin, Pan-cytokeratin = pink; NKG2D = yellow, scale bar = 100 µm). **B.** Representative multiplex IF image of human PDAC showing NK cell-epithelial cell co-localization (Pan-cytokeratin = cyan, NKp46 = yellow, αSMA = magenta, scale bar = 50 µm). **C.** Quantification of percentages of NCAM$^+$ and NKp46$^+$ NK cells and panCK$^+$ epithelial cells from **B** (n = 20). **D.** Cellular interaction analysis (blue = strong avoidance, red = strong interaction; FDR, $p < 0.01$) of IMC-defined cell subpopulations. **E.** Bar plots of mean relative minimum distance to NK cells (pixels) per patient (n = 21) revealed that epithelial cells in PDAC are the

closest to NK cells. Cell populations that were significantly distant from epithelial cells were calculated using a Kruskal-Wallis test (*$p < 0.05$, ***$p < 0.001$, ****$p < 0.0001$). **F.** Network graph of the top 75% of interactions between all IMC-defined cell populations in human PDAC showing epithelial cells and NK cells exist in similar networks.

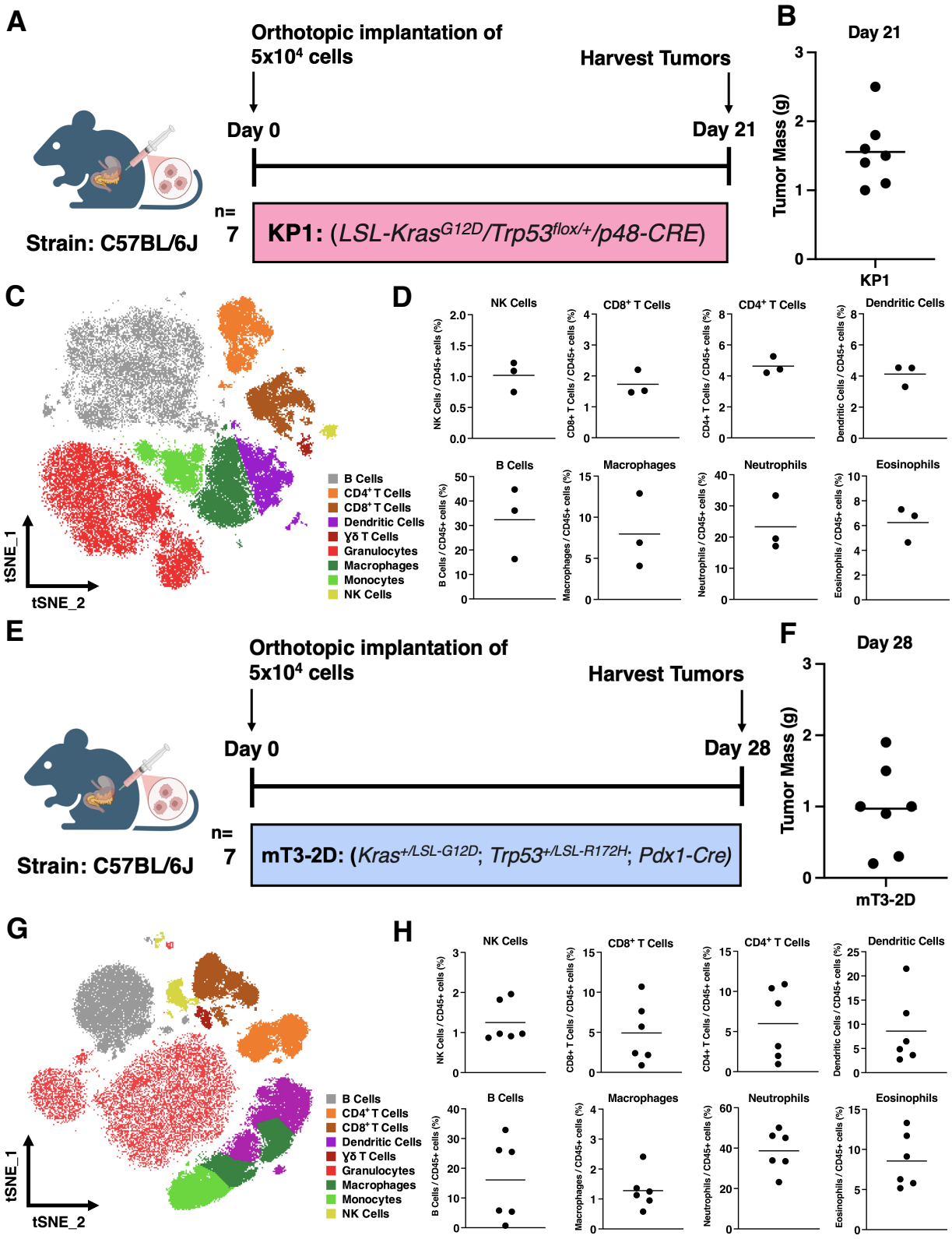
A
Orthotopic implantation of 5x10⁴ cells
Harvest Tumors
Day 0
Day 21
Strain: C57BL/6J
n= 7
KP1: (LSL-KrasG12D/Trp53flox/+/p48-CRE)
B
Day 21
Tumor Mass (g)
KP1
C
tSNE_1
tSNE_2
B Cells
CD4+ T Cells
CD8+ T Cells
Dendritic Cells
γδ T Cells
Granulocytes
Macrophages
Monocytes
NK Cells
D
NK Cells
CD8+ T Cells
CD4+ T Cells
Dendritic Cells
B Cells
Macrophages
Neutrophils
Eosinophils
E
Orthotopic implantation of 5x10⁴ cells
Harvest Tumors
Day 0
Day 28
Strain: C57BL/6J
n= 7
mT3-2D: (Kras+/LSL-G12D; Trp53+/LSL-R172H; Pdx1-Cre)
F
Day 28
Tumor Mass (g)
mT3-2D
G
tSNE_1
tSNE_2
B Cells
CD4+ T Cells
CD8+ T Cells
Dendritic Cells
γδ T Cells
Granulocytes
Macrophages
Monocytes
NK Cells
H
NK Cells
CD8+ T Cells
CD4+ T Cells
Dendritic Cells
B Cells
Macrophages
Neutrophils
Eosinophils

200

201 **Figure 3: Intra-tumoral NK and dendritic cells are in multiple orthotopic, KPC-derived**
202 **murine PDAC models. A.** Schematic representation of *in vivo* experimental design in the KP1
203 tumor model. **B.** Tumor mass at time of analysis (g). **C.** Identification of major immune subsets
204 based on t-SNE plot. **D.** Further quantification of proportion of immune subsets identified via t-
205 SNE analysis (n=3 per group, each dot representing two to three tumors from individual mice).
206 **E.** Schematic representation of *in vivo* experimental design in the mT3-2D tumor model. **F.**
207 Tumor mass at time of analysis (g). **G.** Identification of major immune subsets based on t-SNE
208 plot. **H.** Further quantification of proportion of immune subsets identified via t-SNE analysis
209 (n=6 per group, each dot representing one to two tumors from individual mice).
210
211 **Fibroblast abundance and Collagen I expression excludes NK cells in epithelial-ductal**
212 **regions in the human PDAC TME**
213 While spatial analyses (including neighborhood, interaction, distance, and network
214 modeling) revealed significant colocalization of NK cells with epithelial cells in the human
215 PDAC TME (**Fig. 2**, **Supplementary Figs. S3-S4**), the dense fibroinflammatory stroma
216 characteristic of PDAC—driven by cancer-associated fibroblasts (CAFs)—is known to restrict
217 immune cell infiltration[4]. Therefore, we hypothesized that epithelial-ductal ROIs would show
218 reduced NK cell presence and function. To test this hypothesis, we leveraged previously defined
219 epithelial-ductal regions of interest (ROIs) from our IMC-based cellular neighborhood analysis
220 and used Seurat's[24] CellSelector function to isolate these ROIs for downstream quantification of
221 immune and stromal cell populations (**Supplementary Fig. S3**). Epithelial-ductal ROIs were
222 stratified into 4 quartiles based on their percentage of fibroblast abundance (**Figs. 4A-F**). We
223 confirmed statistically significant increases in fibroblast abundance across the fibroblast

224 abundance quartiles we defined (**Fig. 4C**). As expected, increasing fibroblast abundance was
225 associated with a corresponding rise in Collagen I expression (**Fig. 4D**), consistent with
226 fibroblast-driven matrix deposition. Importantly, NK cell abundance decreased significantly
227 across fibroblast quartiles (**Fig. 4F**), indicating spatial exclusion of NK cells from fibroblast-rich
228 epithelial regions. This exclusion was accompanied by a reduction in NKp44$^+$ and IFNγ$^+$
229 epithelial cells (**Supplementary Fig. S8E**), cell types previously associated with NK cell-
230 enriched neighborhoods (**Supplementary Figs. S3-S4**). These findings suggest that fibroblast
231 accumulation not only limits NK cell infiltration but also attenuates NK cell–epithelial cell
232 interactions and associated cytolytic signaling. In contrast, CD8$^+$ T cell abundance remained
233 unchanged across fibroblast quartiles (**Supplementary Figs. S8-S9**), supporting prior reports of
234 T cell preference for stromal over epithelial compartments in PDAC[25].
235 To determine if decreased NK cell infiltration across fibroblast abundance quartiles
236 correlated with cell functionality, we further evaluated the cellular-based expression of
237 functional markers in NK cell populations within these epithelial-ductal ROIs. We found that NK
238 cells retained expression of activation markers (CD69, CD107a, IFNγ) in low-fibroblast regions,
239 with a notable increase in Granzyme B expression (**Figs. 4G–J**). Furthermore, αSMA$^+$
240 fibroblasts appear responsible for NK exclusion from epithelial ductal regions, with increased
241 αSMA$^+$ fibroblasts associating with reduced NK-tumor cell co-localization (**Figs. 4K-M**). These
242 data demonstrate that NK cells remain functionally competent where they can access epithelial
243 tumor cells, and that their exclusion from fibroblast-rich epithelial ROIs is associated with
244 impaired proximity-dependent cytolytic activity. Together, these findings provide spatial
245 evidence that the desmoplastic stroma in PDAC acts as a physical and functional barrier to NK
246 cell infiltration and effector activity within epithelial compartments. This represents a novel

247 mechanism of immune evasion in PDAC and suggests that stromal remodeling to reduce
248 fibroblast density or collagen deposition may be required to enable effective NK cell-based
249 immunotherapies.
250

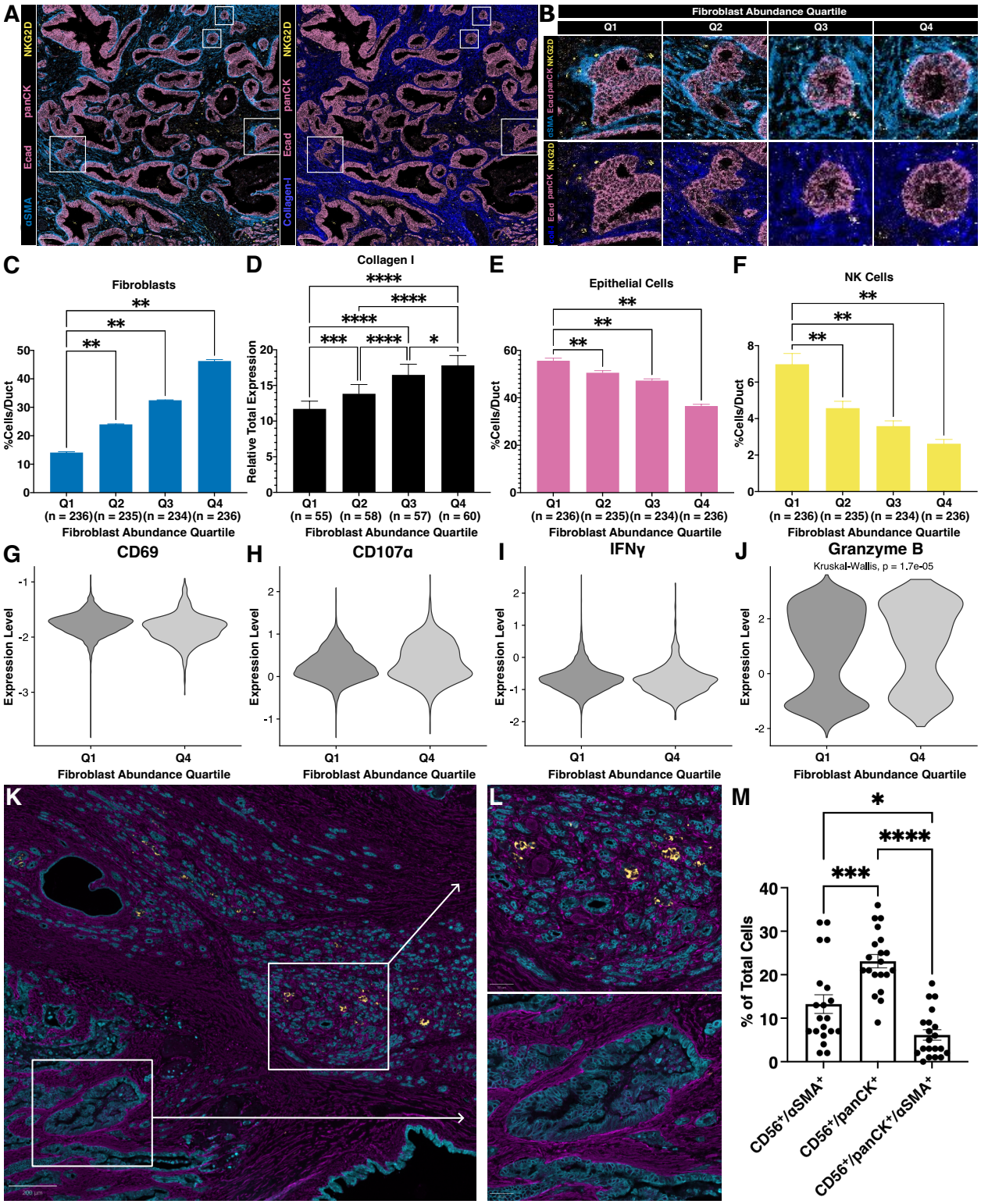

Figure 4: Fibroblast abundance and Collagen I expression exclude NK cells in epithelial-ductal regions in the human PDAC TME. A. Representative IMC pseudoimages showing

αSMA (left, light blue) or collagen-I (right, dark blue) with pan-cytokeratin (panCK, pink), E-cadherin (Ecad, pink), and NKG2D (yellow); scale bar = 100 μm with white boxes of each fibroblast abundance quartile. **B.** Insets of representative epithelial-ductal ROIs from each fibroblast abundance quartile (Q1-Q4) shown in the white insets in **A**. Bar plots of percent cells/ducts (mean ± SEM) of **C.** total fibroblasts, **E.** epithelial cells, and **F.** NK cells in epithelial-ductal ROIs ranked by fibroblast abundance quartile (2-way ANOVA; ****$p < 0.0001$; n = 952, total epithelial-ductal ROIs). **D.** Bar plots of percent cells/ducts (mean ± SEM) of total collagen-I expression in epithelial-ductal ROIs ranked by fibroblast abundance quartile (2-way ANOVA; *$p < 0.05$, ***$p < 0.001$, ****$p < 0.0001$; n = 230, total epithelial ductal ROIs). Violin plots showing NK cell-based expression in Q1 and Q4 fibroblast abundance quartiles of **G.** CD69 **H.** CD107α **I.** IFNγ, and **J.** Granzyme B (Kruskal-Wallis test). **K.** Representative multiplex IF image of human PDAC showing fibroblast exclusion of NK cells in PDAC epithelial-ductal regions (Pan-cytokeratin (panCK) = cyan, NKp46 = yellow, αSMA = magenta, scale bar = 200 μm). **L.** Zoomed insets of **K.** displaying NKp46$^+$/panCK$^+$/αSMA$^+$ and (top) NKp46$^-$/panCK$^+$/αSMA$^+$ (bottom) PDAC epithelial-ductal regions. **M.** Quantification of co-localization of CD56$^+$/αSMA$^+$, CD56$^+$/panCK$^+$, and CD56$^+$/panCK$^+$/αSMA$^+$ cells in PDAC patient samples (Pan-cytokeratin (panCK) = cyan, NKp46 = yellow, αSMA = magenta). One-way ANOVA with Tukey's multiple comparison's test (*$p < 0.05$, ***$p < 0.001$, ****$p < 0.0001$; n = 20).

276 **CellChat identifies CD44 as a potential mediator of interactions between NK cells with**
277 **CAFs and malignant epithelial cells in human PDAC**

278 Since IMC analysis of the PDAC TME demonstrated that NK cells preferentially interact
279 with epithelial cells, and their infiltration is inhibited by fibroblasts, we next further elucidated
280 their potential molecular interactions using CellChat to infer L-R interactions among NK cells,
281 fibroblasts, and epithelial cells. CellChat is a tool with a manually curated database to infer L-R
282 interactions from scRNAseq data[26]. We used this analysis pipeline against a recently published
283 human PDAC scRNAseq dataset containing adjacent-normal (AdjNorm) and PDAC patient
284 samples[27]. Because malignant epithelial cells are typically less differentiated than their normal
285 counterparts[28], we used CytoTRACE—a computational tool that predicts cellular differentiation
286 states from scRNA-seq data[29]—to distinguish malignant from normal epithelial populations
287 (**Supplementary Figs. S10A-C**). To further distinguish potential fibroblast L-R pairs with NK
288 cells, we subclustered fibroblasts to identify known PDAC CAF subpopulations and successfully
289 identified myofibroblasts (myCAFs), inflammatory CAFs (iCAFs), antigen-presenting CAFs
290 (apCAFs), normal fibroblasts, and stellate-like fibroblasts[30] (**Supplementary Figs. S10D-E**).

291 Using CellChat, we assessed the interaction strength of NK cells, fibroblast, and
292 epithelial cell populations to determine which of these populations exhibited significant changes
293 in their outgoing or incoming signaling between AdjNorm and PDAC disease states. CellChat
294 analysis revealed that iCAFs and myCAFs in PDAC exhibited increased outgoing signaling
295 compared to normal adjacent tissue, while NK cells and malignant epithelial cells were
296 prominent signal receivers (**Fig. 5A**). This suggests that CAFs orchestrate interactions amongst
297 these three cell populations in PDAC. Notably, NK cells in PDAC primarily received signals
298 from apCAFs, myCAFs, iCAFs, stellate-like fibroblasts, and malignant epithelial cells (**Fig. 5B**).

299 Among the enriched signaling pathways, the collagen pathway showed the greatest
300 increase in PDAC-specific communication, driven by upregulated collagen expression in CAFs
301 and tumor cells (**Fig. 5C**). Within this pathway, NK cells were targeted by multiple collagen
302 isoforms via CD44, their primary receptor for collagen binding (**Fig. 5D**). Differential expression
303 analysis further showed that CD44 was uniquely upregulated in NK cells within the PDAC
304 TME, while collagen genes were elevated in malignant epithelial cells, iCAFs, and myCAFs
305 (**Fig. 5D, Supplementary Fig. S11**). These findings suggest that NK cells are sequestered within
306 collagen-rich regions via CD44, potentially impairing their directed migration toward tumor
307 targets. Thus, disrupting the CD44–collagen axis may enhance NK cell motility and antitumor
308 function in PDAC.
309

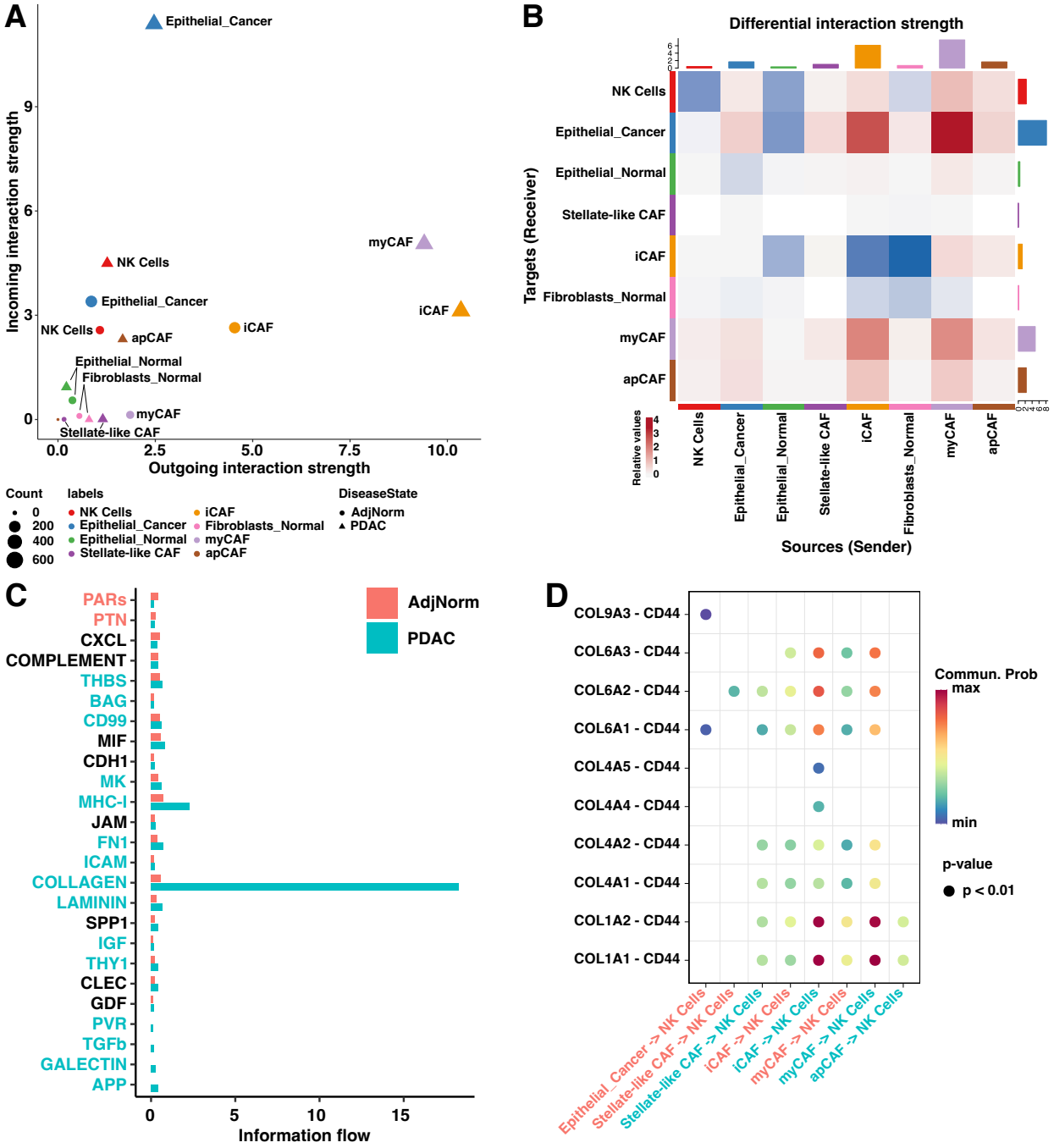

Figure 5: CellChat identifies CD44 as a potential mediator of interactions between NK cells with CAFs and malignant epithelial cells in human PDAC. A. Incoming and outgoing interaction strength for each cell population grouped by AdjNorm and PDAC disease states. **B.** Heatmap of differential interaction strengths of target (y-axis) and source (y-axis) cells with bar plots displaying the absolute values of interactions. **C.** Communication probabilities of signaling

316 pathways targeting NK cells between AdjNorm and PDAC disease states as measured by
317 information flow (pathway legend: pink = AdjNorm-specific, teal = PDAC-specific, black =
318 equally specific). **D.** Significant ligand-receptor pairs from the COLLAGEN signaling pathways
319 targeting NK cells upregulated in PDAC compared to AdjNorm (interaction legend (x-axis): pink
320 = AdjNorm, teal = PDAC).
321
322 **CD44 neutralization increases human donor NK cell invasion *in vitro***
323 The CD44 glycoprotein is highly expressed by a variety of cell types[31]. While its main
324 ligand is hyaluronic acid (HA), which can be highly expressed by cancer and stromal cells[31],
325 CD44 is also known to bind to collagens, laminins, and FN1[32]. CD44 signaling is also known to
326 affect cellular proliferation, adhesion, and migration[31]. Based on CellChat findings, we
327 hypothesized that CD44-mediated binding to ECM components restricts NK cell infiltration in
328 PDAC by anchoring them within the stroma. To test this, we first confirmed CD44 expression of
329 human donor NK cells by flow cytometry (**Supplementary Fig. S12**). We then evaluated NK
330 cell invasion through basement-membrane and collagen-containing matrices *in vitro.* In a 2D
331 Boyden-Chamber Transwell assay, membranes were coated with Matrigel and NK cells were
332 incubated with or without a CD44-neutralizing antibody (α-CD44) (**Fig. 6A**). We found a
333 statistically significant increase in NK cell invasion in three of four human donor NK cell lines
334 upon α-CD44 exposure (**Fig. 6B-E**). To validate these findings in a more physiological context,
335 we employed a 3D *in vitro* model using a tumor spheroid assay (**Fig. 6F**). We generated
336 spheroids using the human PDAC PANC-1 cell line and embedded them with human donor NK
337 cells in a Collagen: Matrigel mixture with or without α-CD44 for 24 hours. After incubation,
338 spheroids were stained by IF and imaged. To assess NK cell infiltration, we used Pan-cytokeratin

339 staining to outline the spheroids and measured NK cell infiltration into PANC-1 spheroids.
340 Again, under conditions of α-CD44 exposure, we observed a statistically significant increase of
341 NK cell invasion using three human donor NK cell lines (**Figs. 6G-K**, **Supplementary Fig.**
342 **S13**).

343 To confirm that neutralizing CD44-collagen binding was responsible for increased NK
344 cell invasion, we explored additional potential mechanisms of action for NK cell invasion.
345 Matrix metalloproteinases (MMPs) are known to degrade ECM, including collagen, and play a
346 role in neutrophil, macrophage, and T cell migration[31,33]. Importantly, MMP expression can be
347 regulated by CD44[31,33]. Thus, we hypothesized that neutralizing CD44-mediated binding by NK
348 cells would increase the expression of matrix metalloproteinases (MMPs). Human donor NK
349 cells were treated for 1 and 4 hours with or without α-CD44, and these cells were assessed for
350 expression of MMP genes (**Supplementary Table S5**). We found no significant differences in
351 MMP gene expression across both exposure conditions (**Supplementary Fig. S14**), strongly
352 suggesting that antibody-based CD44 neutralization mitigates NK cell binding to ECM
353 components to increase NK cell invasion through matrix-containing environments.

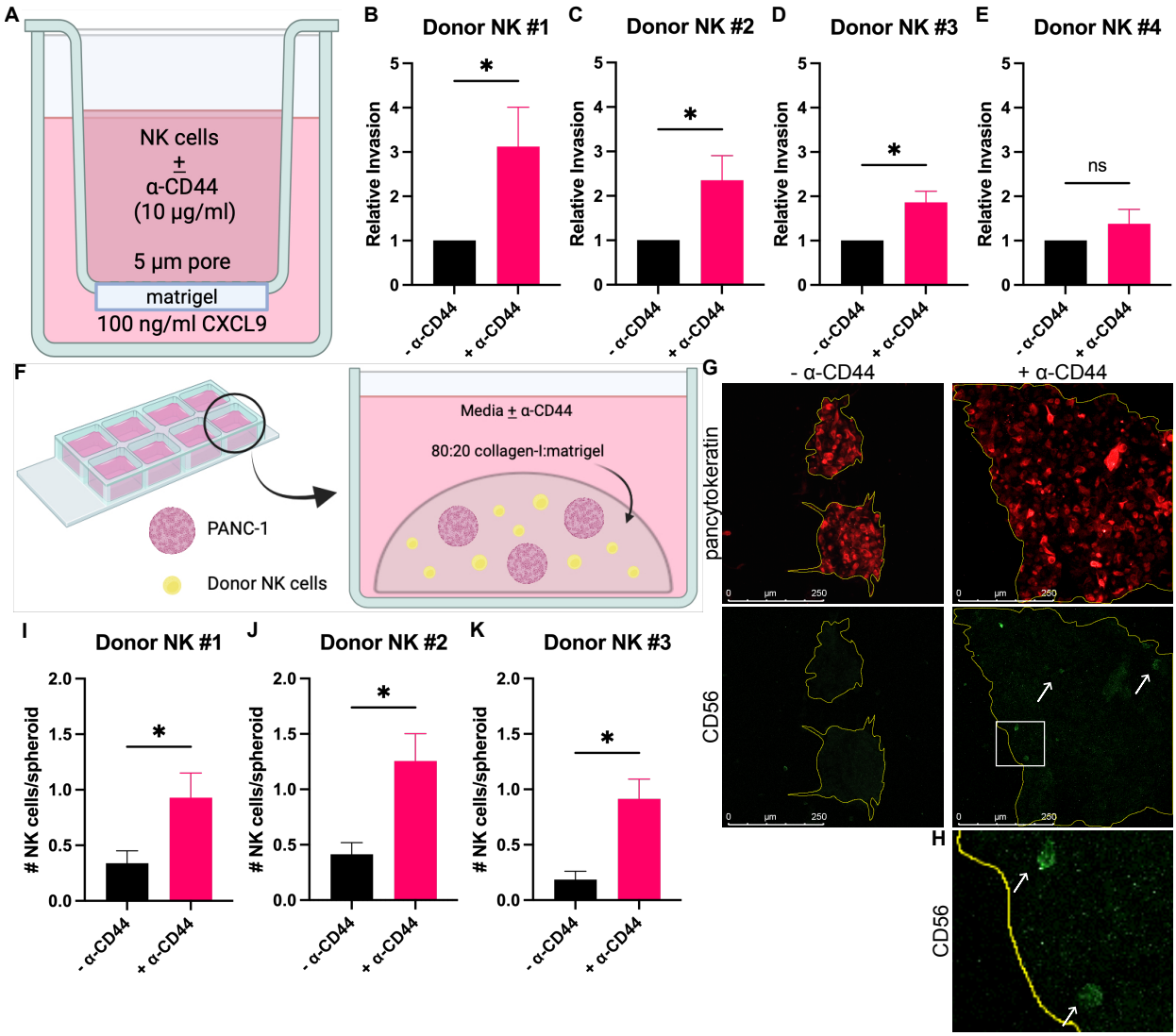

Figure 6: CD44 neutralization increases human donor NK cell invasion *in vitro*. A. Schematic for Transwell invasion assays. Average relative invasion ± SEM of **B.** Donor NK #1 (n = 9), **C.** Donor NK #2 (n = 12), **D.** Donor NK #3 (n = 6), and **E.** Donor NK #4 (n = 10) upon CD44 neutralization. *$p < 0.05$ as determined by Wilcoxon matched-pairs signed rank test. **F.** Schematic of spheroid invasion assay. **G.** Representative 20X IF images of outlined (yellow) PANC-1 spheroids (Pan-cytokeratin; red) embedded with NK cells (CD56; green), pointed out with white arrows, treated with or without α-CD44. Scale bar = 250 µm. **H.** Zoomed inset of NK cells in the α-CD44 treatment group in **G** (white box). Average number of NK cells per PANC-1

363 spheroid ± SEM from **I.** Donor NK #1 (- α-CD44, n = 53; + α-CD44, n = 42), **J.** Donor NK #2 (-

364 α-CD44, n = 29; + α-CD44, n = 43), and **K.** Donor NK #3 (- α-CD44, n = 27; + α-CD44, n =

365 47); n = # of spheroids analyzed; *$p < 0.05$ as determined by Wilcoxon matched-pairs signed

366 rank test.

367 **Discussion**

368 While previous studies have used spatial approaches to examine the PDAC TME
369 landscape[7,25,34], NK cells have not been systematically analyzed using spatial or single-cell
370 approaches. We report for the first time that NK cells are the predominant immune cell type co-
371 localizing with tumor cells in epithelial-ductal regions in PDAC.

372 Here, we utilized three single cell methodologies to further characterize NK cells in
373 human PDAC and multiple murine PDAC models. First, we used an IMC spatial proteomics
374 platform to define the spatial relationships of NK cells within the architecture of the human
375 PDAC TME and defined distinct epithelial, fibroblast, and immune cell populations. We found
376 that active NK cells are abundant in the PDAC TME and form strong cellular relationships with
377 PDAC epithelial cells. Not only are NK cells relatively abundant and active, but they exist in
378 similar proportions to that of T cell populations across patient samples. Multiplex IF imaging
379 further confirmed NK cell co-localization with epithelial cells. Spatial proteomic analysis
380 showed that NK cells, unlike T cells, preferentially localize to epithelial regions of the tumor.
381 NK cells not only co-localized with ductal epithelial cells, but also exhibited direct spatial
382 interactions with apoptotic tumor cells. Distance and network analyses confirmed that epithelial
383 cell populations were the most proximal and strongly connected population to NK cells. Lastly,
384 spatial analysis showed that NK cell localization is inversely proportional to both fibroblast
385 abundance and Collagen I expression in the PDAC TME, suggesting that desmoplasia affects
386 NK cell infiltration in PDAC.

387 Although previous work has primarily compared epithelial-ductal versus stromal-based
388 ROIs[7,35,36], they have not focused on the spatial distribution of NK cells. Our findings provide
389 novel insights into the heterogeneity of the spatial relationships of NK cells in untreated human

390 PDAC, showing that NK cells preferentially localize to epithelial-rich regions, but are restricted
391 from heavily fibrotic zones. Importantly, these analyses were performed on surgically resected
392 primary tumors from untreated patients; hence the spatial and functional relationships of NK
393 cells from metastases or primary tumors in a therapeutic setting may differ and remain to be
394 explored. Nonetheless, our data provide a benchmark of NK cell function and localization in an
395 untreated setting in primary PDAC tumors. Previous work has primarily assessed or leveraged T
396 cells in monitoring patient prognosis or response to different chemotherapies and
397 immunotherapies[37]. Our findings support future development of therapies to leverage the
398 biological properties of NK cells in PDAC.

399 Given the limitations of our spatial proteomics panel, which prioritized tumor and
400 fibroblast markers, we performed additional immune profiling in multiple KPC-derived
401 orthotopic murine PDAC models using CyTOF. This analysis confirmed the presence of NK
402 cells in both the KP1 and mT3-2D models, regardless of their differential T cell infiltration
403 levels. Notably, NK cells constituted a similar fraction of viable $CD45^+$ cells even in the
404 immunologically "cold" KP1 model, suggesting that NK cell infiltration occurs independently of
405 T cells. Dendritic cell analysis highlighted a predominance of cDC2 subsets, with minimal
406 conventional type 1 dendritic cells (cDC1) present, which may explain the high proportion of
407 naïve $CD8^+$ T cells observed. These data underscore the importance of NK cells in the PDAC
408 immune landscape, independent of canonical T cell–dependent pathways. We have previously
409 shown that NK cells contribute to therapeutic efficacy in the mT3-2D model treated with a pan-
410 dipeptidyl peptidase inhibitor, BXCL701, and anti-PD1 (α-PD1) immunotherapy[13]. This
411 combination, now in a Phase II trial for metastatic PDAC, has shown promising early results[38],
412 highlighting the therapeutic potential of harnessing NK cells.

413 Future studies will employ spatial transcriptional profiling of NK cells in the PDAC TME
414 to expand beyond the resolution of the IMC panel used in these studies and to further dissect NK
415 cell communication. Here, we employed CellChat analysis of a human PDAC scRNA-seq
416 dataset[27]. This revealed that NK cells receive strong incoming signals from cancer-associated
417 fibroblasts (CAFs) and malignant epithelial cells, particularly through extracellular matrix
418 (ECM)-related ligands such as collagens, laminins, and fibronectin. CD44, a receptor for
419 multiple ECM components, emerged as the dominant receptor mediating these interactions on
420 NK cells. Differential gene expression analysis further highlighted CD44 as the only ECM
421 receptor significantly upregulated on NK cells within PDAC samples. These findings suggest
422 that CD44 may mediate physical tethering of NK cells within collagen-rich stromal regions,
423 impairing their directed migration toward tumor targets. To test this hypothesis, we performed
424 functional assays using both 2D Transwell invasion and 3D tumor spheroid models.
425 Neutralization of CD44 significantly increased NK cell infiltration through collagen-containing
426 matrices across multiple donors, supporting a role for CD44-ECM binding in limiting NK
427 motility. Importantly, CD44 blockade did not alter MMP expression, indicating that the
428 increased invasion was not due to enhanced matrix degradation but rather the disruption of
429 CD44-mediated adhesion. These results provide direct evidence that CD44 restricts NK cell
430 movement within the ECM-rich TME of PDAC.
431 CD44 is broadly expressed in solid tumors[31] and has been linked to poor prognosis,
432 metastasis, and macrophage recruitment[39,40,41]. While several studies have examined its role in
433 immune cell activation, especially in IL-2/IL-15-activated NK cells[42,43], its involvement in NK
434 cell migration has remained largely unexplored. Notably, a recent pan-cancer analysis identified
435 CD44-mediated interactions as a key axis between fibroblasts and NK cells, particularly in lung

436 cancer, where higher CD44 expression on NK cells correlated with poorer patient outcomes[44,45].
437 These findings align with our observations and support the hypothesis that CD44 limits NK cell
438 trafficking in desmoplastic solid tumors.

439 While CAFs and ECM factors, such as Collagen I, limit NK cell infiltration, specific
440 ablation of these components has been shown to foster immune suppression and accelerate
441 pancreatic cancer progression[46,47]. Additionally, attempting to directly degrade ECM components
442 has not been successful as a clinical strategy for the treatment of metastatic PDAC[48]. Thus,
443 targeting stromal components that impede anti-tumor immune activity is a potentially hazardous
444 approach in desmoplastic tumors, suggesting that blocking interactions between immune cells
445 and stromal components may be more successful. Our work identifies CD44 as a potential key
446 molecular regulator of NK cell localization and provides a mechanistic rationale for targeting
447 CD44 to enhance NK cell infiltration in densely fibrotic solid tumors. Given that NK cells
448 contribute to the anti-tumor efficacy of immunotherapies, such as BXCL701 and α-PD1
449 combinations currently in clinical trials, these findings support the integration of immune cell-
450 ECM interaction targeting strategies into NK-based therapeutic approaches.

451 In summary, we show that NK cells co-localize with tumor epithelial cells in PDAC and
452 that CD44-mediated interactions with the fibrotic stroma restrict NK cell infiltration in PDAC.
453 Disrupting this axis improves NK cell motility *in vitro*, providing a foundation for future studies
454 to enhance NK cell-based immunotherapy in PDAC and potentially other desmoplastic cancers.
455

456 **Methods**

457 **Tissue samples, antibody validation, metal-conjugation, and imaging mass cytometry**

458 **(IMC)**

459 The Lombardi Comprehensive Cancer Center (LCCC) Histopathology & Tissue Shared

460 Resource (HTSR) provided formalin-fixed, paraffin-embedded (FFPE) human PDAC and spleen

461 tissue samples. For IMC, we used a LCCC-curated FFPE human pancreas tissue microarray

462 (TMA) slide series containing 2 mm cores from normal pancreas, pancreatitis, pancreatic

463 neuroendocrine tumors, intraductal papillary mucinous neoplasm, pancreatic mucinous

464 adenocarcinoma, PDAC, colon adenocarcinoma, testicle, tonsil, and placenta samples, and

465 PDAC cell lines. Information for all TMA samples are available at doi:

466 10.5281/zenodo.10582038. The IMC study was restricted to 44 cores from 21 previously

467 untreated PDAC patients who underwent Whipple resections or distal pancreatectomies

468 (**Supplementary Table S2**).

469 For IMC, we designed a metal-conjugated antibody panel. Carrier-free antibodies not

470 commercially metal-conjugated were validated by IF in PDAC or spleen tissue (**Supplementary**

471 **Table S1**). Antibodies with expected expression patterns were metal-conjugated using MaxPar

472 X8 Multimetal Labeling Kits (Standard Bio Tools (SBI); (**Supplementary Table S1**). Metal-

473 conjugation was validated by cytometry by time-of-flight (CyTOF) (Hyperion Imaging System;

474 SBI) at the LCCC Flow Cytometry Shared Resource (FCSR). Metal-conjugated antibody

475 dilutions were optimized in the pancreas TMA prior to final IMC staining at the HTSR. Antigen

476 retrieval and staining was performed (SBI) at the LCCC HTSR, while image acquisition was

477 performed at the LCCC Mass Spectrometry and Analytical Pharmacology Shared Resource. A

478 maximum of 2.25 mm^2 regions of interest (ROIs) on TMA cores were selected, laser-ablated and

479 analyzed by CyTOF to quantitate the metal-conjugated antibodies per ROI, generating multiplex
480 images[49]. All data were collected using the Hyperion Imaging System (SBI) and qualitatively
481 validated in MCD Viewer (v1.0.560.6; SBI) and QuPath softwares (RRID:SCR_018257).
482
483 **IMC image processing, data transformation, and single-cell clustering**
484 Raw IMC data was processed following the widely used ImcSegmentationPipeline[16]
485 (https://github.com/BodenmillerGroup/ImcSegmentationPipeline). In the Ilastik software
486 (RRID:SCR_015246), DNA, E-cadherin, pan-cytokeratin, vimentin, and CD45RO markers were
487 used to pixel-train and generate cell segmentation probability maps for nuclear, cytoplasmic, cell
488 membrane, and background areas in all IMC images, which were imported into CellProfiler to
489 generate cell segmentation masks to then extract single-cell protein expression data using
490 histoCAT[17]. 412,862 cells were identified across 44 images from 21 PDAC patient samples.
491 Extracted IMC-derived single cell data were imported into R (v4.2.1) for downstream
492 computational analyses. histoCAT-derived single cell data files generated are available at doi:
493 10.5281/zenodo.10582038. All scripts adapted from this pipeline for downstream analyses are
494 available at https://github.com/Weiner-Lab/NaturalKillerCells_PDAC. Single cell protein
495 expression data was log-transformed, re-integrated, and clustered using Seurat-based analysis[24].
496 As single cell expression may contain "lateral spillover" into neighboring single cells as a result
497 of cell segmentation[16], we therefore used a supervised clustering approach to phenotype cells
498 based on canonical cellular morphology markers (αSMA, CD3, CD4, CD8α, CD11b, CD16,
499 CD20, CD45RO, CD56, CD68, E-cadherin, FAP, FOXP3, NKG2D, NKp44, pan-cytokeratin,
500 vimentin), we found that a clustering resolution = 0.35 provided distinct immune, fibroblast, and
501 epithelial cell populations. Each cell population was subsetted and re-clustered to identify the

502 functional state of subclusters using the following markers: CD69, CD107α, cleaved-caspase 3,
503 collagen-I, granzyme B, HLA-A/B/C, HLA-A1, IFNγ, Ki67, MICA, PCNA, perforin, PD-1, PD-
504 L1, and TGFβ. All cellular subclusters were reintegrated and annotated based on functional
505 classification: active subpopulations were solely immune cell based and were characterized by
506 high expression of known immune cell activation markers, CD69, CD107α, and/or IFNγ;
507 proliferative cell populations were characterized by high expression of proliferation markers
508 Ki67 and/or PCNA; and inhibitory subpopulations were characterized by high TGFβ expression,
509 which is known to be immune suppressive. Subclustering identified 29 unique cell populations,
510 which were validated visually using the Cytomapper R package and the MCD Viewer software.
511 Seurat objects containing all the PDAC single cell metadata is available at doi:
512 10.5281/zenodo.10582038 and were converted to SingleCellExperiment[16] objects for
513 downstream spatial analyses.
514

515 **IMC spatial analysis**

516 We generated knn-based interaction graphs for the 15-nearest neighbors and used k-
517 means clustering to group cells into 8 distinct cellular neighborhoods using the
518 SpatialExperiment and imcRtools R packages[16]. Using the imcRtools package, permutation test-
519 based cell-cell interaction analysis identified significant interactions or avoidances between cell
520 populations. Using FDR analysis, cell-cell interactions with $p < 0.01$ were considered
521 statistically significant. Based on Euclidean distance metadata, distance and network analyses
522 were performed, as previously described[8]. Seurat's CellSelector function[24] was used to select and
523 quantify cells in epithelial-ductal ROIs of spatial images. From CellSelector, percentages of cell
524 populations in each epithelial-ductal ROI were quantified, and epithelial-ductal ROIs were

525 stratified in quartiles based on fibroblast abundance (Q1 = low fibroblast quartile, Q4 = high
526 fibroblast quartile). Mean total expression of all markers was quantified in representative
527 epithelial-ductal ROIs of pseudoimages using MCD Viewer. Cell-based expression in epithelial-
528 ductal ROIs was performed using Seurat.
529
530 **Multiplex immunohistochemistry**
531 Sections of 5μm thickness were cut from FFPE tissue blocks containing PDAC tumor
532 samples. Patient samples were from 12 males and 8 females with age ranges between 45-88, and
533 had tumor diameters ranging from 0.1-8 cm (**Supplementary Table S3**). Samples were stained
534 for CD56/NCAM1, CD16, NKp46, panCK, αSMA, and CD68 (**Supplementary Table S4**).
535 The slides were baked at 60°, deparaffinized in xylene, rehydrated, washed in distilled
536 water and incubated with 10% neutral buffered formalin (NBF) for an additional 20 minutes to
537 increase tissue-slide retention. Epitope retrieval/microwave treatment (MWT) for all antibodies
538 was performed by boiling slides in the respective Epitope Retrieval buffer (ER1, pH6 or ER2,
539 pH9; Leica Biosystems AR9961 or AR9640, respectively). Protein blocking was performed
540 using antibody diluent/blocking buffer (Akoya, ARD1001EA) for 10 minutes at room
541 temperature. Primary antibody/OPAL dye pairings, staining order and incubation conditions are
542 listed in the table below. The staining was performed using Leica Bond autostainer. Sections
543 were counterstained with spectral DAPI (Akoya FP1490) for 5 min and mounted with ProLong
544 Diamond Antifade (ThermoFisher, P36961) using StatLab #1 coverslips (CV102450). The order
545 of antibody staining and the antibody/OPAL pairing was predetermined using general guidelines
546 and the particular biology of the panel. General guidelines include spectrally separating co-
547 localizing markers and separating spectrally adjacent dyes. Multiplex IHC was optimized by

548 first performing single-plex IHC with the chosen antibody/OPAL dye pair to optimize signal
549 intensity values and proper cellular expression, followed by optimizing the full multiplex assay.
550 Slides were scanned at 10X magnification using the Phenoimager Fusion system Automated
551 Quantitative Pathology Imaging System (Akoya Biosciences). Whole slide scans were viewed
552 with Phenochart (Phenochart 2.2.0, Akoya) which also allows for the selection of high-powered
553 images at 20X (resolution of 0.5mm per pixel) for multispectral image capture. Multispectral
554 images of each tissue specimen were captured in their entirety.

555 Additional human PDAC samples were used for multiplex IF to assess panCK, E-
556 cadherin, CD56, and NKG2D (**Supplementary Fig. S2**, **Supplementary Table S3**). Patient
557 samples were from 4 males and 2 females with age ranges between 44-86, and had tumor
558 diameters ranging from 3.7-18 cm.

559 Multiplex staining and imaging were performed as previously described[50], except tissue
560 images were captured using Akoya Biosciences Inc.'s PhenoImager Fusion imaging platform at
561 the LCCC HTSR. Images were exported as *.qtiff* files and visualized using QuPath software
562 (RRID:SCR_018257).

563

564 **Single-cell RNA-sequencing analysis**

565 To infer ligand-receptor (L-R) interactions in PDAC, we utilized a previously published
566 human PDAC scRNAseq dataset[27] and subsetted NK cells, fibroblasts, and epithelial cells.
567 Malignant and normal epithelial cells were differentiated using CytoTRACE, a computational
568 framework that predicts cellular differentiation states by measuring the number of genes
569 expressed by each cell[29]. The CytoTRACE scores distribution was observed to be bi-modal and
570 using a mixed-model, an ideal cut-off value separating the two distributions was determined to

571 be 0.72 where scores greater than 0.72 indicated a malignant epithelial cells[51] (**Supplementary**
572 **Fig. S10**). Fibroblasts were subclustered into known subpopulations and we identified: antigen-
573 presenting CAFs (apCAFs), inflammatory CAF (iCAFs), myofibroblasts (myCAFs), normal
574 fibroblasts, and stellate-like fibroblasts[30] (**Supplementary Fig. S10**). We then used CellChat, a
575 manually curated protein database of approximately 2,000 L-R pairs[26] to infer potential L-R
576 interactions between epithelial, fibroblast, and NK cell populations. A Wilcox test with a
577 Bonferroni correction from the FindMarkers Seurat function (v4.3) was used for differential gene
578 expression analysis of CellChat-identified L-R genes. Genes with an adjusted-$P < 0.01$ were
579 considered significantly differentially expressed. R scripts for applied CytoTRACE and CellChat
580 analyses are available at https://github.com/Weiner-Lab/NaturalKillerCells_PDAC.
581

582 **Cell culture**

583 Human PANC-1 PDAC cells and donor NK cell lines were cultured, as previously
584 described[52], except donor NK cells received 0.5% v/v of IL-2. Healthy human donor NK cell
585 lines, Donor NK #1, #2, and #4 were purchased (STEMCELL Technologies, Vancouver,
586 Canada), and Donor NK #3 cells were isolated from a leukoreduction system (LRS) chamber
587 (Inova Health System) and isolated via MojoSortTM Human NK Cell Isolation Kit (BioLegend,
588 CAT#: 480053). Donor NK cells were stimulated with the engineered K562 cell line
589 (RRID:CVCL_0004), K562-mb21-41BBL (courtesy of Dr. Dean Lee at Nationwide
590 Children's)[53]. K562-mb21-41BBL cells were cultured in supplemented RPMI (10% FBS, 1%
591 penicillin/streptomycin). For NK cell stimulation, K562-mb21-41BBL cells were collected (5
592 minutes, 1,000 rpm, 4˚C), resuspended in supplemented RPMI with mitomycin C (Sigma-
593 Aldrich) (C_f = 0.01 mg/ml) and incubated for 4 hours (37˚C). Pre-treated K562-mb21-41BBL

594 cells were collected (5 minutes, 1,000 rpm, 4˚C), resuspended in NK cell medium, then co-
595 cultured with donor NK cells (E:T = 1:1); this process was repeated at least once per week.
596 Donor NK cells aged day 1-50 and stimulated 1-3 days prior to *in vitro* assays were used. The
597 mT3-2D murine pancreatic cancer cell line was a gift from David Tuveson, Cold Spring Harbor
598 Laboratory, Lauren Hollow, New York, USA[54]. The KP1 murine pancreatic cancer cell line was
599 a gift from David DeNardo, Washington University School of Medicine, St. Louis, USA[55]. Cells
600 were cultured in supplemented DMEM media (10% FBS). All cell lines were tested and
601 determined to be free of mycoplasma and murine cell lines were free of other rodent pathogens.
602
603 **Flow cytometry**
604 Cells were centrifuged (5 minutes, 1,000rpm, 4˚C) washed twice (1X PBS), then
605 resuspended in FACS staining buffer (1% BSA in 1X PBS). Human Fc block (BD Pharmigen,
606 CAT#: 564219) then α-CD44-BV605 (BioLegend, CAT#: 103047) antibodies were added per
607 manufacturer's recommendations (30 minutes, 4˚C). Cell pellets were washed twice (FACS
608 staining buffer), resuspended in fixative (1% PFA in 1X PBS), then processed by the LCCC
609 FCSR in a BD LSRFortessa Cell Analyzer (BD Biosciences). Analysis was performed using
610 FlowJo (v10.8.1; RRID:SCR_008520).
611
612 **NK cell 2D invasion assay**
613 The bottom of 5 µm Transwells (Corning) were coated with Matrigel (Corning) diluted
614 1:3 in NK cell medium. CXCL9 (C_f =100 ng/ml) (R&D Systems)-supplemented NK cell
615 medium was added to the bottom of each well. Donor NK cells were added to Transwells with or
616 without an α-CD44 neutralizing antibody (clone IM7; Bio X Cell; C_f = 10 µg/ml) and incubated

617 for 4 hours (37˚C). Transwells were removed, cells were stained with Trypan Blue Stain (Gibco)
618 and manually counted on a hemocytometer. Control cells were plated without Transwells to
619 count total cells to calculate percent invasion. Relative invasion is the percent of cells that
620 invaded through the transwell normalized to untreated NK cell conditions. A Wilcoxon matched-
621 pairs signed rank test was performed to determine statistical significance (GraphPad Prism v10;
622 RRID:SCR_002798).
623
624 **NK cell 3D spheroid invasion assay**
625 As previously described,[27] PANC-1 cells were seeded in each well of a low-adhesion U-
626 bottom plate, spun (5 minutes, 1,000 rpm, 4˚C) and cultured overnight. Spheroids were
627 embedded with donor NK cells in an 80:20 Collagen-I (Invitrogen): Matrigel (Corning) mixture
628 in chamber wells (Lab-Tek). Embedded spheroids were treated with α-CD44 (clone IM7; Bio X
629 Cell; C_f = 10 μg/ml) for 24 hours (37˚C) prior to immunocytochemistry (IC). For IC, samples
630 were fixed with 4% paraformaldehyde (PFA; 10 minutes, 25˚C), washed with 1X PBS (5
631 minutes), then permeabilized with 0.5% Triton-X100 (10 minutes). Cells were washed once,
632 blocked (1% BSA in 1X PBS, 30 minutes), then incubated with human Fc block (BD Pharmigen,
633 CAT#: 564219). Samples were incubated with pan-cytokeratin-eFluor™ 660 (Invitrogen, CAT#:
634 50-9003-82) and CD56 (Invitrogen, CAT#: MA1-19129) antibodies overnight (25˚C). An α-
635 Mouse IgG2a-AF488 secondary antibody (Invitrogen, CAT#: A-21131; 1-4 hours, 25˚C), cells
636 were washed 3 times, incubated with DAPI (50 ng/ml; 10 minutes, 25˚C), then washed twice.
637 Coverslips were mounted with anti-fade mountant, then and dried. Z-stacks of spheroids were
638 imaged using a Leica SP8 AOBS microscope at the LCCC Microscopy and Imaging Shared
639 Resource. Z-stacks were ≤ 1 μm. Z-stack images were processed and using FIJI software[56]

640 (v2.14.0; RRID:SCR_002285) for manual NK cell quantitation into PANC-1 spheroids.
641 Statistical significance was determined using a Wilcoxon matched-pairs signed rank test
642 (GraphPad Prism v10).
643
644 **Effects of CD44 neutralization on MMP gene expression in human NK cells**
645 Donor NK cell lines were incubated with or without α-CD44 (clone IM7; Bio X Cell; C_f
646 = 10 µg/ml) for 1 and 4 hours. Cells were collected (5 minutes, 1,000 rpm, 4˚C) and RNA was
647 isolated using the PureLink™ RNA Mini Kit (Ambion). RNA concentration was measured using
648 NanoDrop 8000 (ThermoFisher Scientific), then stored at -80˚C. Diluted RNA (20 ng/µl) was
649 treated with 10% v/v 10X DNase I Buffer and 10% v/v DNase I (Promega; 15 minutes, 25˚C).
650 10% v/v of RQ1 RNase/DNase Stop Solution (Promega) and 10% v/v Oligo(dT) nucleotides
651 (IDT) were added, then heat inactivated at 65˚C (10 minutes) then at 4˚C (5 minutes). cDNA was
652 synthesized with the GoScript™ Reverse Transcriptase Kit (Promega). qPCR was performed
653 using GoTaq qPCR Master Mix (Promega) with the StepOnePlus™ Real-Time PCR System
654 (ThermoFisher Scientific). Gene expression was quantified ($2^{-\Delta C_T}$; Ambion) using *HPRT*
655 (Forward 3'→5': CTTTCCTTGGTCAGGCAGTA, reverse 3'→5':
656 TGGCTTATATCCAACACTTCG) as an internal, endogenous control. Fold-change was
657 calculated using the $2^{-\Delta\Delta C_T}$ method and a One-Way ANOVA, Kruskal-Wallis test was performed
658 to determine statistical significance (GraphPad Prism v10).
659
660 **Animal studies**
661 C57BL/6J (female, 7 weeks old) mice were purchased from The Jackson Laboratory (Bar
662 Harbor, Maine, USA). All studies involving animals were reviewed and approved by the

663 Georgetown University Institutional Animal Care and Use Committee (GU IACUC). KP1 and
664 mT3-2D cells were grown in antibiotic-free DMEM with 10% FBS for at least 2 passages prior
665 to implantation. Orthotopic PDAC tumors were established as briefly described. In brief, the left
666 side of the mouse abdomen was shaved, mice were anesthetized using isoflurane and a small, 1
667 cm incision was made to access the pancreas. Tumor cells, either $5x10^4$ KP1 or $5x10^4$ mT3-2D,
668 were injected into the pancreas using a 27-gauge needle. Successful injection was verified by the
669 appearance of a fluid bubble without intraperitoneal leakage. The abdominal wall was closed
670 with 4-0 PGA absorbable sutures (Med Vet International, Mettawa, IL, USA) and the skin was
671 closed with 4-0 nylon non-absorbable sutures (Stoelting Co., Wood Dale, IL, USA). Wound clips
672 (Stoelting Co., Wood Dale, IL, USA) were then used to secure skin sutures. Mice were
673 euthanized with CO_2 inhalation at designated endpoint or when mice showed signs of pain or
674 distress, whichever came first. Tumors were harvested, weighed, and dissociated into a single
675 cell suspension for subsequent CyTOF analysis.
676
677 **CyTOF analysis**
678 CyTOF analysis was performed using previously described protocols and gating
679 strategies[22,23]. Single cell suspensions were prepared as previously described[21]. Briefly, single
680 cell suspensions were obtained from fresh tumor tissue by incubation with a mixture of RPMI-
681 1640 media containing 10% FBS and 1 mg/mL Collagenase D (11088858001, Sigma Aldrich)
682 with shaking at 150 rpm for 40 mins at 37 ^{o}C and then filtering through a 70 μM strainer.
683 Samples were incubated with antibodies according to the MaxPar OnDemand Mouse Immune
684 Profiling Panel Kit (Standard BioTools, San Francisco, CA, USA) and loaded onto a CyTOF
685 System (Helios, Standard BioTools, San Francisco, CA, USA) for signal detection and single

686 cell analysis. Data was normalized and then exported. Viable $CD45^+$ cells were identified for
687 each sample. Each sample was down sampled (DownSample v3.3.1, FlowJo) to 33,333
688 individual cells and samples were concatenated. Batch correction was performed using
689 CyCombine (CyCombine 1.0.2, FlowJo). The tSNE was then applied to identify cell populations.
690 GraphPad Prism 10.0 was used for visualizing results. Gating was done using FlowJo software
691 (v10.8.1).
692
693 **Ethics statement**
694 The human pancreas TMA and PDAC slides used in this study were approved by the
695 Georgetown University LCCC Biospecimen Use Committee. Animal studies were reviewed and
696 approved by the Georgetown University Institutional Animal Care and Use Committee
697 (IACUC).

698 **Supplementary Materials**

699 Supplementary Figure S1: Subclustered cell populations of spatial proteomic resolved PDAC
700 cell populations.

701 Supplementary Figure S2: NK cells co-localize with PDAC epithelial cells.

702 Supplementary Figure S3: Cellular neighborhood analysis identifies distinct epithelial-ductal
703 structural regions, containing both NK cells and epithelial cells, in the human PDAC TME.

704 Supplementary Figure S4: Proportions of PDAC subclustered cell populations per cellular
705 neighborhood.

706 Supplementary Figure S5: Expression levels of immune markers on tSNE plots.

707 Supplementary Figure S6: CyTOF gating strategy for murine PDAC tumors.

708 Supplementary Figure S7: Functional characterization of immune populations identified via
709 tSNE analysis.

710 Supplementary Figure S8: PDAC epithelial-ductal ROI cell subcluster abundance.

711 Supplementary Figure S9: PDAC epithelial-ductal ROI cell type abundance.

712 Supplementary Figure S10: Subclustering of epithelial and fibroblast populations in human
713 PDAC scRNAseq samples.

714 Supplementary Figure S11: Fibroblast and epithelial cell populations exhibit differential
715 expression of CellChat-based collagen signaling genes.

716 Supplementary Figure S12: Human donor and murine NK cells express CD44.

717 Supplementary Figure S13: CD44 neutralization increases human donor NK cell invasion into
718 PANC-1 PDAC spheroids

719 Supplementary Figure S14: CD44 neutralization does not affect expression of MMP genes in
720 human donor NK cells

721 Supplementary Table S1: IMC antibody panel and metal assignments.

722 Supplementary Table S2: PDAC patient information for IMC.

723 Supplementary Table S3: PDAC patient information for multiplex IF (Vectra®).

724 Supplementary Table S4: Antibodies and fluorescent dyes for multiplex IF (Vectra®).

725 Supplementary Table S5: MMP genes primer sequences.

Acknowledgments

We would like to thank the following from the Georgetown University Lombardi Comprehensive Cancer Center's Shared Resources (SR) (partially supported by NIH/NCI P30CA51008 grant): Dr. Karen Creswell, Dan Xu, and Zhinuo Jiang at the Flow Cytometry and Cell Sorting SR (partially supported NIH S10OD016213 grant), Aaron Rozeboom, Bin Li, and Susree Modepalli at the Histopathology and Tissue SR, Dr. Junfeng Ma at the Mass Spectrometry and Analytical Pharmacology and the Biostatistics SR for support with performing metal-conjugation, IMC, and multiplex immunofluorescence, and with providing guidance on spatial analyses. We would also like to thank the Tissue Culture and Biobanking and Microscopy and Imaging Shared Resources for support on *in vitro* assays. We also thank Ahmed Elhossiny and the Pasca Di Magliano lab at the University of Michigan for providing us with the scRNAseq dataset for analyses described here. We also thank Drs. Andrew Quong and Eric Swanson at Standard BioTools Inc. for assistance with the IMC antibody panel design and its cell segmentation pipeline, and Dr. Ludmila Danilova at Johns Hopkins University for advice on computational analyses. Schematics were created with BioRender.com.

Author contributions

Z.X.M., A.A.L., and L.M.W. conceived the idea, designed the study, obtained funding, and wrote the manuscript. Z.X.M. and A.A.L. conducted experiments and analyzed the data. Z.X.M., R.K.S., A.D., S.A., and W.J.H. performed or assisted with computational analyses. Z.X.M., R.K.S., and S.A. wrote R scripts and generated the computational figures. B.H. and A.D. assisted with data collection and tissue pathology of human tissue samples. A.A.L., S.A., R.M., A.J.L., A.Z., and M.A., assisted with *in vivo* experiments. L.W. and M.C. assisted in performing 2D *in*

749 *vitro* invasion experiments. M.C. assisted with RT-qPCR, flow cytometry assays, and 3D *in vitro*
750 invasion experiments. I.P. and S.H. assisted in IMC data collection. W.J.H., E.J.F., M.A., and
751 S.A.J. assisted with experimental design. All authors critically reviewed and approved the
752 manuscript.
753
754 **Competing interests**
755 The authors have no competing interests to declare.
756
757 **Code availability statement**
758 Code used to perform IMC and scRNAseq analyses and generate the figures is available at
759 https://github.com/Weiner-Lab/NaturalKillerCells_PDAC.
760
761 **Data transparency statement**
762 Code used to perform IMC and scRNAseq analyses and generate the figures is available at
763 https://github.com/Weiner-Lab/NaturalKillerCells_PDAC. Raw .mcd files for all cores of the
764 pancreas tissue microarray imaged by IMC and IMC-derived datasets, including histoCAT-
765 derived single cell files, and Seurat, SingleCellExperiment, Cytomapper and distance data matrix
766 R objects, to reproduce figures are deposited at doi: 10.5281/zenodo.10582038. Source Data are
767 provided with this paper. The scRNAseq data was provided to us by the Pasca Di Magliano lab
768 at the University of Michigan, which was previously published at doi: 10.1038/s43018-020-
769 00121-4. The authors declare that all other data supporting the findings of this study are available
770 within the paper or its supplementary information files. All other relevant data are available from
771 the corresponding author upon request.

Funding

This work is supported by grants from the National Institutes of Health, National Cancer Institute T32CA009686 (Training Grant in Tumor Biology, Anna Tate Riegel), F31CA261125 (Z.X.M.), F30CA294875 (A.A.L.), and P30CA51008 (L.M.W), and Achievement Reward for College Scientists (ARCS) Foundation Scholar (Z.X.M.).

References

1 Siegel, R. L., Giaquinto, A. N. & Jemal, A. Cancer statistics, 2024. *CA: a cancer journal for clinicians* **74**, 12-49 (2024). https://doi.org:10.3322/caac.21820

2 Caputo, D. Hot topics in pancreatic cancer management. *World Journal of Gastrointestinal Surgery* **15**, 121 (2023). https://doi.org:10.4240/wjgs.v15.i2.121

3 Karamitopoulou, E. Tumour microenvironment of pancreatic cancer: immune landscape is dictated by molecular and histopathological features. *British journal of cancer* **121**, 5-14 (2019). https://doi.org:10.1038/s41416-019-0479-5

4 Muller, M. *et al.* The immune landscape of human pancreatic ductal carcinoma: key players, clinical implications, and challenges. *Cancers* **14**, 995 (2022). https://doi.org:10.3390/cancers14040995

5 Ferdek, P. E. & Jakubowska, M. A. Biology of pancreatic stellate cells—more than just pancreatic cancer. *Pflügers Archiv-European Journal of Physiology* **469**, 1039-1050 (2017).

6 Malchiodi, Z. X. & Weiner, L. M. Understanding and Targeting Natural Killer Cell-Cancer-Associated Fibroblast Interactions in Pancreatic Ductal Adenocarcinoma. *Cancers (Basel)* **13** (2021). https://doi.org:10.3390/cancers13030405

7 Liudahl, S. M. *et al.* Leukocyte heterogeneity in pancreatic ductal adenocarcinoma: phenotypic and spatial features associated with clinical outcome. *Cancer discovery* **11**, 2014-2031 (2021). https://doi.org:10.1158/2159-8290.cd-20-0841

8 Ho, W. J. *et al.* Neoadjuvant cabozantinib and nivolumab convert locally advanced hepatocellular carcinoma into resectable disease with enhanced antitumor immunity. *Nature Cancer* **2**, 891-903 (2021). https://doi.org:10.1038/s43018-021-00234-4

9 Le Rochais, M., Hemon, P., Pers, J.-O. & Uguen, A. Application of high-throughput imaging mass cytometry hyperion in cancer research. *Frontiers in Immunology* **13**, 859414 (2022). https://doi.org:10.3389/fimmu.2022.859414

10 Chang, Q. *et al.* Biodistribution of cisplatin revealed by imaging mass cytometry identifies extensive collagen binding in tumor and normal tissues. *Scientific reports* **6**, 36641 (2016). https://doi.org:10.1038/srep36641

11 Kuett, L. *et al.* Three-dimensional imaging mass cytometry for highly multiplexed molecular and cellular mapping of tissues and the tumor microenvironment. *Nature Cancer* **3**, 122-133 (2022). https://doi.org:10.1038/s43018-021-00301-w

12 Sheng, J. *et al.* Topological analysis of hepatocellular carcinoma tumour microenvironment based on imaging mass cytometry reveals cellular neighbourhood regulated reversely by macrophages with different ontogeny. *Gut* **71**, 1176-1191 (2022). https://doi.org:10.1136/gutjnl-2021-324339

13 Fitzgerald, A. A. *et al.* DPP inhibition alters the CXCR3 axis and enhances NK and CD8+ T cell infiltration to improve anti-PD1 efficacy in murine models of pancreatic ductal adenocarcinoma. *J Immunother Cancer* **9** (2021). https://doi.org:10.1136/jitc-2021-002837

14 Chang, Q. *et al.* Imaging mass cytometry. *Cytometry part A* **91**, 160-169 (2017). https://doi.org:10.1002/cyto.a.23053

15 Iyer, A., Hamers, A. & Pillai, A. CyTOF® for the masses. Front Immunol (13): 815828. *Frontiers in immunology* **13**, 815828 (2022). https://doi.org:10.3389/fimmu.2022.815828

16 Windhager, J. *et al.* An end-to-end workflow for multiplexed image processing and analysis. *Nature Protocols*, 1-49 (2023). https://doi.org:10.1038/s41596-023-00881-0

17 Schapiro, D. *et al.* histoCAT: analysis of cell phenotypes and interactions in multiplex image cytometry data. *Nature methods* **14**, 873-876 (2017). https://doi.org:10.1038/nmeth.4391

18 Hafemeister, C. & Satija, R. Normalization and variance stabilization of single-cell RNA-seq data using regularized negative binomial regression. *Genome biology* **20**, 296 (2019). https://doi.org:10.1186/s13059-019-1874-1

19 Schürch, C. M. *et al.* Coordinated cellular neighborhoods orchestrate antitumoral immunity at the colorectal cancer invasive front. *Cell* **182**, 1341-1359. e1319 (2020). https://doi.org:10.1016/j.cell.2020.07.005

20 Mi, H., Ho, W. J., Yarchoan, M. & Popel, A. S. Multi-scale spatial analysis of the tumor microenvironment reveals features of cabozantinib and nivolumab efficacy in hepatocellular carcinoma. *Frontiers in immunology* **13**, 892250 (2022). https://doi.org:10.3389/fimmu.2022.892250

21 Ajina, R. *et al.* Antitumor T-cell immunity contributes to pancreatic cancer immune resistance. *Cancer immunology research* **9**, 386-400 (2021). https://doi.org:10.1158/2326-6066.CIR-20-0272

22 Tang, T. *et al.* Transcriptional control of pancreatic cancer immunosuppression by metabolic enzyme CD73 in a tumor-autonomous and-autocrine manner. *Nature Communications* **14**, 3364 (2023). https://doi.org:10.1038/s41467-023-38578-3

23 Han, G., Spitzer, M. H., Bendall, S. C., Fantl, W. J. & Nolan, G. P. Metal-isotope-tagged monoclonal antibodies for high-dimensional mass cytometry. *Nature protocols* **13**, 2121-2148 (2018). https://doi.org:10.1038/s41596-018-0016-7

24 Hao, Y. *et al.* Integrated analysis of multimodal single-cell data. *Cell* **184**, 3573-3587. e3529 (2021). https://doi.org:10.1016/j.cell.2021.04.048

25 Carstens, J. L. *et al.* Spatial computation of intratumoral T cells correlates with survival of patients with pancreatic cancer. *Nat Commun* **8**, 15095 (2017). https://doi.org:10.1038/ncomms15095

26 Jin, S. *et al.* Inference and analysis of cell-cell communication using CellChat. *Nature communications* **12**, 1088 (2021). https://doi.org:10.1038/s41467-021-21246-9

27 Steele, N. G. *et al.* Multimodal mapping of the tumor and peripheral blood immune landscape in human pancreatic cancer. *Nature cancer* **1**, 1097-1112 (2020). https://doi.org:10.1038/s43018-020-00121-4

28 Enane, F. O., Saunthararajah, Y. & Korc, M. Differentiation therapy and the mechanisms that terminate cancer cell proliferation without harming normal cells. *Cell death & disease* **9**, 912 (2018). https://doi.org:10.1038/s41419-018-0919-9

29 Gulati, G. S. *et al.* Single-cell transcriptional diversity is a hallmark of developmental potential. *Science* **367**, 405-411 (2020). https://doi.org:10.1126/science.aax0249

30 Zhang, T., Ren, Y., Yang, P., Wang, J. & Zhou, H. Cancer-associated fibroblasts in pancreatic ductal adenocarcinoma. *Cell Death Dis* **13**, 897 (2022). https://doi.org:10.1038/s41419-022-05351-1

31 Chen, C., Zhao, S., Karnad, A. & Freeman, J. W. The biology and role of CD44 in cancer progression: therapeutic implications. *Journal of hematology & oncology* **11**, 1-23 (2018). https://doi.org:10.1186/s13045-018-0605-5

32 Guo, Q., Yang, C. & Gao, F. The state of CD44 activation in cancer progression and therapeutic targeting. *The FEBS Journal* **289**, 7970-7986 (2022). https://doi.org:10.1111/febs.16179

866 33 McMahon, M., Ye, S., Pedrina, J., Dlugolenski, D. & Stambas, J. Extracellular matrix
867 enzymes and immune cell biology. *Frontiers in Molecular Biosciences* **8**, 703868 (2021).
868 https://doi.org:10.3389/fmolb.2021.703868
869 34 Hwang, W. L. *et al.* Single-nucleus and spatial transcriptome profiling of pancreatic cancer
870 identifies multicellular dynamics associated with neoadjuvant treatment. *Nature genetics* **54**, 1178-
871 1191 (2022). https://doi.org:10.1038/s41588-022-01134-8
872 35 Birnbaum, D. J. *et al.* Transcriptomic analysis of laser capture microdissected tumors
873 reveals cancer-and stromal-specific molecular subtypes of pancreatic ductal adenocarcinoma.
874 *Clinical Cancer Research* **27**, 2314-2325 (2021). https://doi.org:10.1158/1078-0432.CCR-20-
875 1039
876 36 Yousuf, S. *et al.* Spatially resolved multi-omics single-cell analyses inform mechanisms of
877 immune dysfunction in pancreatic cancer. *Gastroenterology* **165**, 891-908. e814 (2023).
878 https://doi.org:10.1053/j.gastro.2023.05.036
879 37 Hester, R., Mazur, P. K. & McAllister, F. Immunotherapy in pancreatic adenocarcinoma:
880 beyond "copy/paste". *Clinical Cancer Research* **27**, 6287-6297 (2021).
881 https://doi.org:10.1158/1078-0432.CCR-18-0900
882 38 Weinberg, B. A. *et al.* Phase II trial of BXCL701 and pembrolizumab in patients with
883 metastatic pancreatic ductal adenocarcinoma (EXPEL-PANC): Preliminary findings. *ASCO*
884 *Annual Meeting* **42**, Abstract LBA4132 (2024).
885 https://doi.org:10.1200/JCO.2024.42.17_suppl.LBA4132
886 39 Liu, S. *et al.* CD44 is a potential immunotherapeutic target and affects macrophage
887 infiltration leading to poor prognosis. *Scientific Reports* **13**, 9657 (2023).
888 https://doi.org:10.1038/s41598-023-33915-4
889 40 Rios De la Rosa, J. M., Tirella, A., Gennari, A., Stratford, I. J. & Tirelli, N. The CD44-
890 mediated uptake of hyaluronic acid-based carriers in macrophages. *Advanced healthcare materials*
891 **6**, 1601012 (2017). https://doi.org:10.1002/adhm.201601012
892 41 Vey, N. *et al.* Phase I clinical study of RG7356, an anti-CD44 humanized antibody, in
893 patients with acute myeloid leukemia. *Oncotarget* **7**, 32532 (2016).
894 https://doi.org:10.18632/oncotarget.8687
895 42 Paul, S. & Lal, G. The molecular mechanism of natural killer cells function and its
896 importance in cancer immunotherapy. *Frontiers in immunology* **8**, 1124 (2017).
897 https://doi.org:10.3389/fimmu.2017.01124
898 43 Sconocchia, G., Titus, J. A. & Segal, D. M. Signaling pathways regulating CD44-
899 dependent cytolysis in natural killer cells. *Blood, The Journal of the American Society of*
900 *Hematology* **90**, 716-725 (1997). https://doi.org:10.1182/blood.V90.2.716
901 44 Nagao, F., Suzui, M., Takeda, K., Yagita, H. & Okumura, K. Mobilization of NK cells by
902 exercise: downmodulation of adhesion molecules on NK cells by catecholamines. *American*
903 *Journal of Physiology-Regulatory, Integrative and Comparative Physiology* **279**, R1251-R1256
904 (2000). https://doi.org:10.1152/ajpregu.2000.279.4.r1251
905 45 Netskar, H. *et al.* Pan-cancer profiling of tumor-infiltrating natural killer cells through
906 transcriptional reference mapping. *Nature Immunology* **25**, 1445-1459 (2024).
907 https://doi.org:10.1038/s41590-024-01884-z
908 46 Özdemir, B. C. *et al.* Depletion of carcinoma-associated fibroblasts and fibrosis induces
909 immunosuppression and accelerates pancreas cancer with reduced survival. *Cancer cell* **25**, 719-
910 734 (2014). https://doi.org:10.1016/j.ccr.2014.04.005

47 Chen, Y. *et al.* Type I collagen deletion in αSMA+ myofibroblasts augments immune suppression and accelerates progression of pancreatic cancer. *Cancer cell* **39**, 548-565. e546 (2021). https://doi.org:10.1016/j.ccell.2021.02.007

48 Van Cutsem, E. *et al.* Randomized phase III trial of pegvorhyaluronidase alfa with nab-paclitaxel plus gemcitabine for patients with hyaluronan-high metastatic pancreatic adenocarcinoma. *Journal of Clinical Oncology* **38**, 3185-3194 (2020). https://doi.org:10.1200/JCO.20.00590

49 Delgado-Gonzalez, A. & Sanchez-Martin, R. M. Mass cytometry tags: where chemistry meets single-cell analysis. *Analytical Chemistry* **93**, 657-664 (2020). https://doi.org:10.1021/acs.analchem.0c03560

50 Lee, C.-W. *et al.* Multiplex immunofluorescence staining and image analysis assay for diffuse large B cell lymphoma. *Journal of immunological methods* **478**, 112714 (2020). https://doi.org:10.1016/j.jim.2019.112714

51 Scrucca, L., Fop, M., Murphy, T. B. & Raftery, A. E. mclust 5: clustering, classification and density estimation using Gaussian finite mixture models. *The R journal* **8**, 289 (2016). https://doi.org:10.32614/RJ-2016-021

52 Zahavi, D. J. *et al.* Antibody dependent cell-mediated cytotoxicity selection pressure induces diverse mechanisms of resistance. *Cancer Biology & Therapy* **24**, 2269637 (2023). https://doi.org:10.1080/15384047.2023.2269637

53 Carr, W. H., Zinsou, C., Rowe, T., Lange, C. & Lawal, O. O. Human natural killer cell expansion in vitro using mitomycin-C treatment as an alternative to irradiation of modified K562 feeder cells. *The Journal of Immunology* **198**, 82.16-82.16 (2017). https://doi.org:10.4049/jimmunol.198.Supp.82.16

54 Boj, S. F. *et al.* Organoid models of human and mouse ductal pancreatic cancer. *Cell* **160**, 324-338 (2015). https://doi.org:https://doi.org/10.1016/j.cell.2014.12.021

55 Jiang, H. *et al.* Targeting focal adhesion kinase renders pancreatic cancers responsive to checkpoint immunotherapy. *Nature medicine* **22**, 851-860 (2016).

56 Schindelin, J. *et al.* Fiji: an open-source platform for biological-image analysis. *Nature methods* **9**, 676-682 (2012). https://doi.org:10.1038/nmeth.2019